sustainability

MDPI

Article

Multimodal Monitoring of Corrosion in Reinforced Concrete for Effective Lifecycle Management of Built Facilities

Subhra Majhi [1], Leonarf Kevin Asilo [1], Abhijit Mukherjee [1,*], Nithin V. George [2] and Brian Uy [3]

[1] School of Civil and Mechanical Engineering, Curtin University, Bentley, WA 6102, Australia
[2] Department of Electrical Engineering, Indian Institute of Technology, Gandhinagar 382355, Gujarat, India
[3] School of Civil and Environmental Engineering, University of Sydney, Camperdown, NSW 2006, Australia
* Correspondence: abhijit.mukherjee@curtin.edu.au

Abstract: Monitoring the corrosion of steel rebars is paramount to ensuring the safety and serviceability of reinforced concrete (RC) structures. Conventional electro-chemical techniques can provide an overall estimate of the extent of corrosion. However, a detailed account of the extent of corrosion would help in understanding the residual strength of corroding RC structures. A passive wave-based technique such as acoustic emissions can identify the location of corrosion but always requires the presence of transducers on the structure. In active wave-based techniques, the structure is excited through a pulse excitation and their subsequent response to this excitation is measured. Thus, for active techniques, the transducers need not always be present in the structure. In guided wave ultrasonics, the excitation pulse is imparted through a waveguide to determine the state of corrosion. This technique relies on parameters such as time of flight or attenuation of the incident signal to predict the state of corrosion. These parameters can be susceptible to uncertainties in the transducer of ultrasonic coupling. In the present study, concrete specimens with embedded steel bars have been subjected to accelerated corrosion. They have been monitored with a combination of active and passive techniques. The received signals are analyzed through a modified S-Transform-based time-frequency approach to obtain a range of modes that propagate through the specimen. The changes in the modal composition of the guided wave signals due to corrosion are parameterized and correlated to various stages of corrosion. A holistic understanding of the stages of corrosion is developed by the inclusion of acoustic emission hits to guided wave parameters. Based on the Guided Wave Ultrasonics and acoustic emission parameters, corrosion has been classified into Initiation, Intermediate, and Advanced. Subsequently, destructive tests have been performed to measure the residual strength of the corroded bars. Thus, this paper presents a novel proof of concept study for monitoring corrosion with Guided Wave Ultrasonics and acoustic emissions.

Keywords: guided wave ultrasonics; longitudinal waves; pulse excitation; time-frequency analysis; modified S-Transforms; reinforced concrete; acoustic emissions; corrosion monitoring

Citation: Majhi, S.; Asilo, L.K.; Mukherjee, A.; George, N.V.; Uy, B. Multimodal Monitoring of Corrosion in Reinforced Concrete for Effective Lifecycle Management of Built Facilities. *Sustainability* **2022**, *14*, 9696. https://doi.org/10.3390/su14159696

Academic Editor: Antonio Caggiano

Received: 7 June 2022
Accepted: 1 August 2022
Published: 6 August 2022

1. Introduction

The construction industry alone is responsible for 7% of global CO_2 emissions among other Green House Gases (GHG) [1]. As the world-built infrastructure is aging, emissions associated with the restoration and replacement of existing facilities are increasing rapidly. An estimated A$47 billion worth of Australian infrastructure assets are in poor or very poor condition and need immediate repair [2]. A vast majority of built concrete infrastructure suffers from corrosion of reinforcing bars [3]. This is especially vivid in the case of Australia, where more than 85% of the population lives within 50 km of the coastline. Corrosion in concrete infrastructure, if undetected, increases maintenance costs throughout the lifecycle of the structure. Delays in corrosion detection would result in subsequent delays in maintenance. Thus, delays in early intervention would be detrimental to the service life of the structure. Regular and reliable inspection of infrastructure is thus imperative to avoid detrimental economic and environmental costs associated with the replacement of structures. Recent developments in wave technologies and advanced signal processing promise advancements in reliability and economy in corrosion monitoring of structures.

During the initial service life of concrete, its high alkalinity protects the reinforcement bars from corrosion [4]. Exposure to a chloride-rich environment decreases the pH of concrete. Corrosion of steel manifests with the development of a layer of corrosion products around the rebar. The corrosion products fill up the rebar-concrete layer, exerting a bursting pressure on the surrounding concrete. This results in the nucleation of cracks [5]. Subsequently, corrosion escalates with the disintegration of the corrosion product layer and the pitting of the rebar. This severely reduces the strength and ductility of the reinforcing bar [6,7]. This makes early detection and monitoring of corrosion in concrete structures imperative for their maintenance [8,9]. Condition assessment methods, such as Impact Echo [10] and Infrared Thermography [11], have been reported for monitoring corrosion but are mostly suitable for detecting cracks in concrete. Electrochemical methods have been reported for understanding corrosion in concrete structures. The likelihood of corrosion can be predicted by electrochemical measurements [6,12,13] and the extent of it.

Traveling waves based on their interaction with the propagating media can provide a quantitative overview of their condition [14–16]. Corrosion of reinforcement in concrete uniquely affects the surface of the rebar and the surrounding concrete. The extent of corrosion can be monitored through these waves through the reinforcement or the surrounding concrete [17–19]. Their efficacy can be improved by using an active-guided wave-based system [20,21]. Using the steel rebar as a waveguide, the condition of the steel–concrete interface can be determined [22,23].

The temporal characteristics of guided wave signals have predominantly been utilized to discern the condition of the waveguide. The essence of variation in these modes is understood in terms of variation in Time of Flight (ToF) and signal attenuation [24–26]. Changes to the waveguides can be correlated to unique changes in propagation modes in traveling guided waves [27,28]. Traveling wave velocities, energy distribution, and attenuation characteristics unique to waveguides can be understood through the dispersion relationship [29,30]. These relations have been used to identify guided wave modes that are sensitive to damage to the core and surface of the waveguide reinforcing bar [17,18]. This has resulted in the characterization of guided-wave modes sensitive to different stages of corrosion [31,32]. However, the uncertain coupling between the transducers and the substrate can be a challenge unless advanced signal processing is used [33,34].

Supplementing frequency information to the temporal signal spectra enhances understanding of the signal [35]. Short-Time Fourier Transform (STFT) can reveal the association between the temporal and frequency characteristics of the signal [36]. Improvements in the localization of time-frequency spectra have been achieved by replacing the fixed time window with a variable one [37]. Some variants of time-frequency analysis have been reported in flaw detection [38,39], de-bond detection in plates [40], crack propagation [41], and measurement of strain levels [42]. The present authors have demonstrated an improved S-Transform-based technique that monitors corrosion in steel bars by observing the shifts in dominant frequencies with time [43]. A proof of concept validation of improvement in signal spectra through advanced signal processing monitoring corrosion or steel bars can be demonstrated [43,44]. The efficacy of guided wave signals in corrosion monitoring is better understood when they are correlated with acoustic signals [45].

Acoustic transducers can be installed on concrete structures as a passive method of monitoring corrosion [46–48]. They have been used to detect and classify corrosion in lab-scale specimens [49–51]. It is imperative to select transducers of a suitable frequency range for data acquisition. Past research indicates corrosion produces acoustic activity in the frequency range of 20–80 kHz [52]. Signal analysis of these acoustic waves has discerned different features, such as the development of microcracks, localized crack propagation, and debonding of the reinforcing steel during corrosion. Thus, acoustic activity has been correlated to the determination of the onset of corrosion and nucleation of concrete cracking during corrosion [53]. An amalgamation of active and passive wave-based schemes will result in a nuanced monitoring technique [54].

This paper provides a proof-of-concept advanced signal processing paradigm based on S-Transform to monitor corrosion in reinforcing bars in concrete. Several RC specimens have been cast. They have been subjected to accelerated corrosion at varying levels. The specimens were excited with an ultrasonic pulse to generate a guided wave through the steel bar. An improved method of extracting the time-frequency spectra from the acquired ultrasonic data is reported. Variation in the signal due to advancing corrosion in the rebar embedded in concrete is monitored. The state of corrosion in the rebar is classified and correlated with acoustic emissions. These readings have been calibrated with destructive tests of the rebars.

2. Experimental Program

Figure 1 shows the experimental program. It has three phases: (1) preparation of specimens; (2) subjecting them to accelerated corrosion while monitoring them with ultrasonic guided waves and acoustic emissions; and (3) destructive tests. Standard reinforced concrete specimens have been cast and cured in a water bath for 28 days. They have been loaded in flexure to create a crack in the tension zone of the concrete. They have been subjected to accelerated corrosion by applying a specified anodic current. After corrosion exposure, the bars have been extracted out of the concrete and subjected to destructive tests.

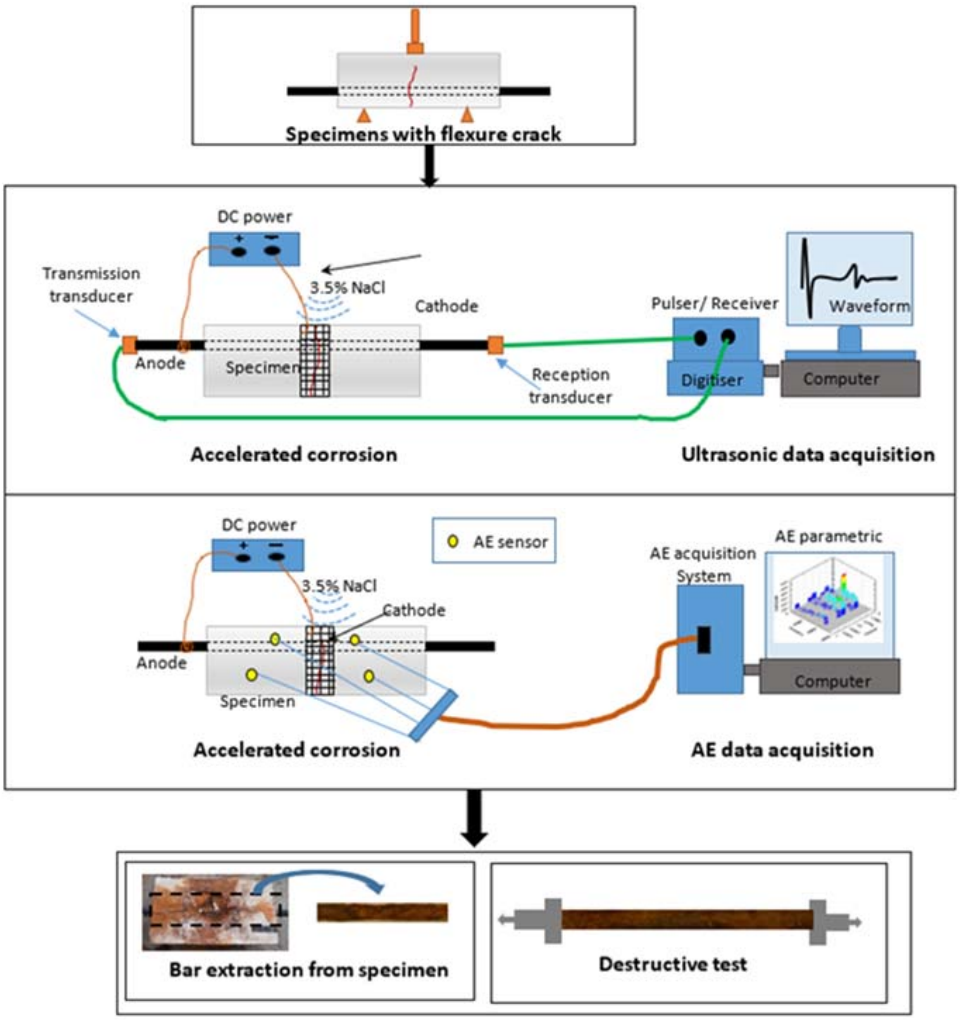

Figure 1. Schematic of the experimental paradigm and non-destructive monitoring of the specimen subjected to accelerated corrosion followed by destructive tests.

2.1. Specimen Preparation

Concrete specimens of dimensions 500 × 250 × 150 mm were prepared. A mild steel bar of 24 mm diameter and 900 mm length was placed in the mold. Before placement in the mold, the bar was cleaned with a wire brush and weighed. A concrete mix as specified in Table 1 was prepared. The specimens S_{corr1} and S_{corr2} were cast to be monitored with Guided Wave Ultrasonics and acoustic emissions, respectively. The maximum coarse aggregate size in the mix was 10 mm. The mold was filled with the concrete mix and vibrated in a table vibrator. After the initial setting of concrete, the specimens were cured in a water bath for 28 days. After the curing period, they were kept in ambient conditions to dry. To establish the strength of the cast concrete, cylinders were cast with the same mix design. The average compression strength of the concrete after 28 days was found to be 53.1 MPa.

Table 1. Mix design composition of concrete.

Constituent	Cement	Fine Aggregates	Coarse Aggregates	Water-Cement Ratio
Composition	1	1.6	3.4	0.5
Mass (kg/m^3)	370	591	1255	185

After curing, the concrete specimens were prepared for flexural cracks. This was achieved by applying three-point bending. The specimens were placed securely in a universal testing machine and a central point load through a roller was applied. Loading was continued until a clear crack of width ~1 mm was visible at the center of the beam. Loading was stopped at this point. At the time of unloading, the crack closed substantially. However, a clear thin crack was visible on the unloaded sample. The specimen was prepared for accelerated corrosion and simultaneous monitoring with guided wave ultrasonics.

2.2. Accelerated Corrosion

For accelerated corrosion, the specimens (S_{corr1} and S_{corr2}) were wrapped around their central region with a cotton gauze sheet. A stainless-steel wire mesh was wound over this fabric sheet. Water containing a 3.5% NaCl solution was used as a drip on the samples. The salt concentration was selected close to the salinity level of ocean water, emulating marine conditions. A DC power supply was applied to accelerate the process of corrosion. The positive end of the cell was connected to the exposed steel bar and the negative end was connected to the wire mesh. Thus, the wire mesh acts as the cathode and the steel bar acts as the anode (Figure 2). A constant 20 V DC was maintained across the electrodes for 43 days. The specimen S_{corr1} was monitored with guided wave ultrasonics and the specimen S_{corr2} was monitored with acoustic emissions. Both were subjected to similar conditions of accelerated corrosion.

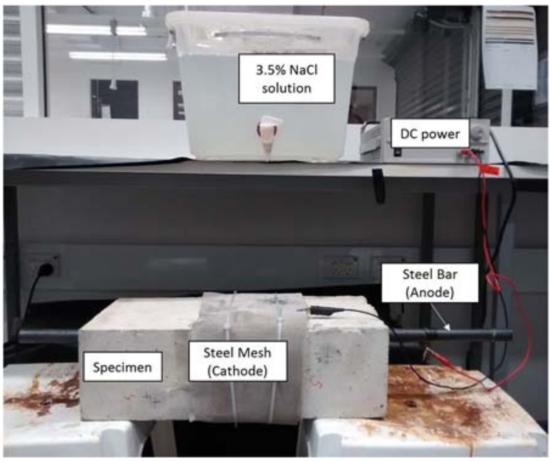

Figure 2. Experimental setup for inducing accelerated corrosion.

2.3. Guided Wave Ultrasonic Monitoring

Simultaneously, regular ultrasonic monitoring was performed as shown in Figure 1. Piezo transducers of make Olympus IMS were pressed securely on both ends of the steel bar using petroleum jelly as a coupler. A pulser-receiver-based function generator to make JSR Ultrasonics was used to send a pulse excitation for the transducers. The signal was digitized by a modular oscilloscope, Picoscope V6.4.64.0. A pulse was generated as an input to the piezo transducers at an input voltage of 475 V. The pulse comprises sinusoids, which are harmonics with generally odd multiples of the primary excitation frequency. Thus, the pulse excitation results in the generation of higher frequency components along with the primary excitation frequency. This enables excitation and access to a group of guided wave modes at one time. The ultrasonic data were acquired in a pitch-catch mode in the form of a time-series plot, which comprised variation of the voltage with time. This was termed an 'A-Scan'. The variation in signal characteristics with advancing corrosion was monitored.

2.4. AE Emission Test

Acoustic Emission (AE) relies on the detection of acoustic energy released from the nucleating cracks [48]. Piezo acoustic sensors tuned to a specific resonant frequency attached to the specimen are used to record the waveform and classify them. The manifestation of corrosion generates acoustic activity in a frequency range of 20–80 kHz [45,52]. As the layer of corrosion products builds up between the bar and concrete, it exerts a bursting pressure on the concrete, thereby causing cracks in the surrounding concrete. These propagating cracks cause acoustic activity that is detected by the acoustic sensors. In the present study, acoustic data were acquired with the AE express acquisition setup of make Physical Acoustics. The acoustic signals from the specimen were acquired with 6 RL6α sensors with a resonant frequency of 60 kHz. The sensors were attached to the specimen with a silicone grease coupling between the sensor and the substrate. The acquired signals were boosted through a pre-amplifier with a set gain of 40 dB to enhance its signal strength before the reception. The arrangement of acoustic sensors for the present experimental scheme is shown in Figure 3.

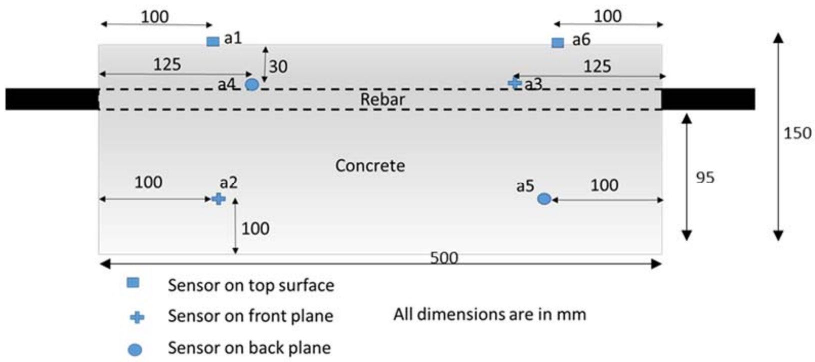

Figure 3. Details of specimen geometry including the physical location of acoustic sensors on the specimen S_{corr2}.

From the acquired acoustic data, the state of corrosion has been classified using acoustic parameters such as hits, counts, energy, events, signal strength and rise time, etc. [55]. These parameters were extracted from the AE waveforms displayed in Figure 4. Hit count corresponds to the recording of an AE hit that exceeds a set signal threshold parameter like amplitude or frequency. Acoustic hits that are picked up by multiple sensors are called an Event. Signal duration represents the time for which a hit remains above this set threshold. Signal strength represents the area of the AE signal expressed in pico-Volt-sec. The energy associated with an identified hit is expressed as Absolute energy in attoJoules (aJ) units. Input parameters for the software in terms of Peak Definition Time (PDT), Hit Definition Time (HDT), and Hit Lockout Time (HLT) in 'µs' are shown in Table 2.

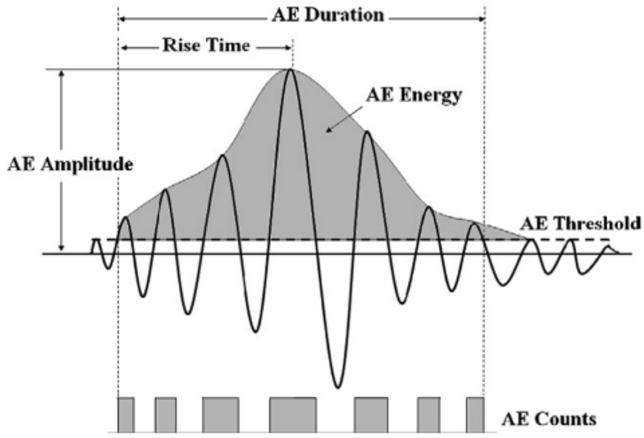

Figure 4. Characteristic AE signal (Reprinted with permission from [47]).

Table 2. Acoustic Emission parameters used in the experiment.

Threshold	Timing Parameters		
	PDT	HDT	HLT
40 dB	200	800	1000

2.5. Destructive Tests

To perform destructive tests, the steel bars were extracted from the concrete, and they were thoroughly cleaned. Mass loss due to corrosion was determined by weighing the specimens. The bars were subjected to a tension test in a universal testing machine to determine the load–deflection relationships. Mechanical properties such as stress–strain relation, yield stress, and ultimate stress have been determined. Their subsequent variation with corrosion was associated.

3. Experimental Results

3.1. Time Signal (A-Scan)

The time-series signals recorded for the pristine specimen are shown in Figure 5. Two peaks nearby can be observed around 165 µs and 200 µs. They correspond to the first arrival of the incident waves at the receiving transducer. Other minor peaks at 300 µs and 500 µs are also observed. In the present work, variation in signal traits in the first and second peaks will be analyzed. The A-Scans are normalized for the absolute maximum value. It is worth noting that these two peaks occur in very close proximity to each other. Thus, the nature of these peaks requires further analysis.

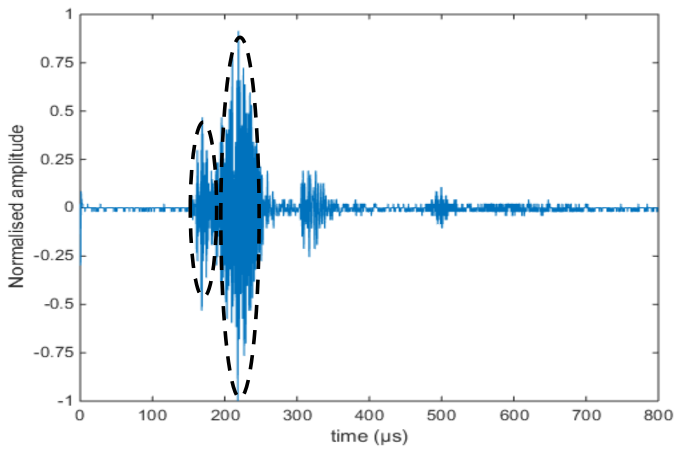

Figure 5. A-Scan recorded for S_{corr1} at Day 0.

3.2. Signal Analysis

Time-frequency analysis is to be applied to the acquired time signals to determine the veracity of dominant frequencies for their arrival times. It should be noted that the present signal analysis paradigm is aimed at alleviating limitations associated with the amplitude-based guided wave systems. This is undertaken by using a windowed function to chunk the acquired signal and subsequently localizing the frequency content in this window. A conventional Fourier Transform in its continuous form is expressed as per Equation (1).

$$X(f) = \int_{-\infty}^{\infty} x(t)e^{-i2\pi ft}dt \tag{1}$$

Here, '*x(t)*' is the temporal representation of the signal, '*f*' represents the frequency, and '*t*' represents the time in the acquired signal. A window function to localize the frequency components for their temporal occurrence is conducted through time-frequency analysis. The Conventional Short Term Fourier Transform (STFT) suffers from poor temporal and frequency resolution as it uses a fixed window to localize the occurrence of dominant frequencies. Improvement can be achieved by using a sliding window. In S-Transform, this window is selected to be a Gaussian. The S-Transform of a time-domain signal can be expressed as per Equation (2).

$$S(\tau, f) = \int_{-\infty}^{\infty} x(t)w(t-\tau)e^{-i2\pi ft}dt \tag{2}$$

Here, the Gaussian window can be expressed in the form of Equation (3).

$$w(t,\sigma) = \frac{1}{\sqrt{2\pi}\sigma}e^{\frac{-(t-\tau)^2}{2\sigma^2}} \tag{3}$$

Further improvement to this Gaussian Window is achieved by varying its standard deviation proportional to the frequency being localized as per the relation: $\sigma = 1/\mid f \mid$. The modified Gaussian window is presented in Equation (4). As this window contracts for higher frequencies and dilates for lower frequencies, the signal is better localized in terms of its time-frequency spectra than that in STFT.

$$w(t-\tau, f) = \frac{|f|}{\sqrt{2\pi}}e^{\frac{-1}{2}[\frac{f(t-\tau)}{l}]^2} \tag{4}$$

In S-Transforms, the Gaussian envelope (Equation (4)) localizes the time while the oscillatory exponential kernel ($e^{-i2\pi ft}$) selects the frequency being localized. The time-frequency spectra are better localized in two ways: first, by the oscillatory exponential kernel which localizes the real and imaginary components of the spectrum independently; second, by the inclusion of the phase and amplitude spectrum of the acquired signal.

The original S-Transform has an indigent time resolution at a lower frequency with an enlarged window and indigent frequency resolution at a higher frequency with a contracted window. The introduction of a scaling factor to adapt to the width of the Gaussian window is the novelty of the present Modified S-Transform. The Gaussian Window is modified with a linearly scaling factor, which is a function of the frequency being localized [56] as per Equation (5).

$$\gamma(f) = \eta f + b \tag{5}$$

With these modifications, the modified S-Transform is presented in Equation (6):

$$S(\tau, f, \eta, b) = \int_{-\infty}^{\infty} x(t)\Psi(f)\exp(\alpha)dt \tag{6}$$

where

$$\Psi(f) = \frac{|f|}{\sqrt{2}\pi(\eta f + b)} \text{ and } \alpha = -\left(\frac{(t-\tau)^2 f^2}{2(\eta f + b)^2} + i2\pi f t\right) \tag{7}$$

The scaling factor ($\gamma(f)$) used to obtain Equation (6) is expressed in terms of parameters 'a' and 'b'. They are selected through trial and error to best suit the results. Thus, the scaling factor proposed in Equation (5) is modified based on the parameters to form Equation (8).

$$\gamma(f) = \frac{a}{N} * f + b \tag{8}$$

Here, $f = [1, 2, \ldots N/2]$ with N represents the length of the time signal.

As the data were acquired in discrete form, the above equations are transformed into a discrete form. The time signal sampled at N uniformly distributed data points is expressed in terms of $[lT]$ discrete points with $l = 0, 1, 2 \ldots (N-1)$ and T represents a single time step in the discretized domain. Using the discrete form of Equation (5), the S-Transform of the discrete signal ($h[lT]$) can be expressed as Equation (9).

$$S\left[\frac{k}{NT}, uT\right] = \sum_{m=0}^{N-1} H\left[\frac{k+m}{NT}\right] W(k,n) exp\left(\frac{-i2\pi mk}{N}\right) \tag{9}$$

where m, k, u, and n = 0, 1, 2, $N-1$ represent the indices for time translation, discrete frequency, number of time steps, and frequency shift, respectively.

Here, *H[k/NT]* is the Fourier transform of the signal $h[lT]$. The discrete frequency transform used in Equation (9) can be expressed as per Equation (10):

$$H\left[\frac{k}{NT}\right] = \frac{1}{N}\sum_{u=0}^{N-1} h[uT] e^{\frac{-i2\pi uk}{N}} \tag{10}$$

The window function used to extract the frequency being localized is conducted through the windowed function as per Equation (11):

$$W(k,n) = exp\left(\frac{-2\pi^2 k^2 \left(\frac{a}{N} * k + b\right)^2}{n^2}\right) \tag{11}$$

The contrast in the time-frequency plot obtained from Equation (9) is further improved by the application of a Contrast Amelioration filter. This filtering scheme is applied to the modified S-Transform spectra as a product of the Fourier Spectra (Equation (10)) with the magnitude spectra of modified S-Transforms (Equation (9)). The resulting Contrast Amelioration Filter can be expressed as per Equation (12).

$$S_{ca}\left[\frac{k}{NT}, uT\right] = \left|S\left[\frac{k}{NT}, uT\right]\right| * H\left[\frac{k}{NT}\right] \tag{12}$$

To ascertain suitable values of parameters a and b resulting in the accurate localization of time and frequency spectra, a series of numerical trials were conducted. The scaled Gaussian window was calculated as per Equation (12). Previous research indicates that the scaling factors a and b usually lie between 1 to 100 and 0.01 and 1, respectively [57]. A broader value of a and b results in relatively narrower windows for the frequencies being localized. Initial trials with a = 20 and b = 1 have resulted in windows as per Figure 6i. Here, the window is presented in the frequency domain as a single-sided Gaussian distribution respective to the frequency index (k). There is an ambiguity regarding arrival with different frequency components of the signal. The higher and lower frequency components appear to have their predominant arrival time between 180 and 250 µs (Figure 6ii). The temporal locations of higher frequency components as indicated are inaccurate. Thus, the parametric values of a, b used for this plot warrant re-examination. Alleviation of temporal inaccuracies associated with the parameters needs to be addressed.

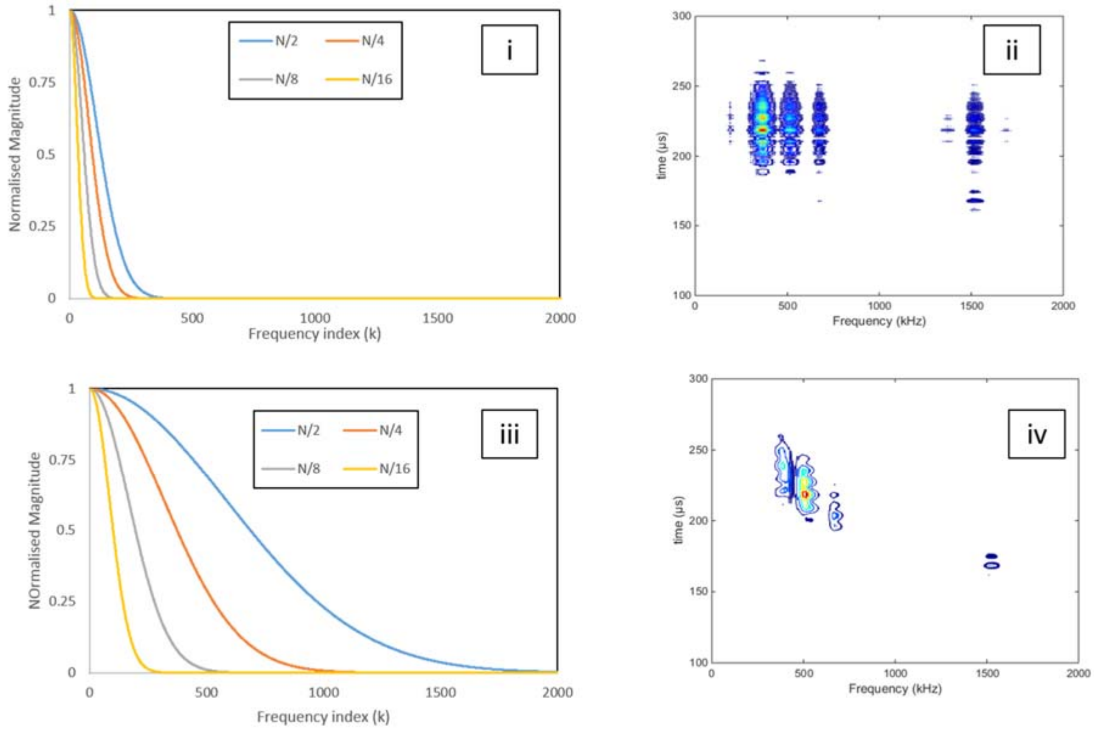

Figure 6. Effect of variation in localization window widths on time-frequency spectra. Variation in $\gamma(f)$: (**i**) a = 20, b = 1; (**iii**) a = 1, b = 0.1 and their corresponding time-frequency spectra (**ii**) a = 20, b = 1; (**iv**) a = 1, b = 0.1.

Assignment of smaller values to the parameter a, b—viz., 1, and 0.1, respectively—have resulted in wider windows for the frequencies being localized (Figure 6iii). Improved localization in the time of arrival of both lower and higher frequencies can be observed. The frequency resolution of the higher frequencies is now affected. The spectral energy corresponding to the higher frequency components is almost negligible in Figure 6iv. Thus, inaccuracies in the localization of higher frequency components can be noticed. The parametric value for 'a' and 'b' lies in between these two regions, which require further investigation.

Several numerical trials were conducted past this point to ascertain the values of a and b between the values considered in Figure 7. A comparison of window widths for the frequency being localized reveals the selection of a = 10 and b = 0.5 as best suited for the present case. It is essential to understand the dilation extent of these windows around different frequencies being localized. Table 3 summarizes some cases which are used to understand the effect of window width dilation for specific frequencies.

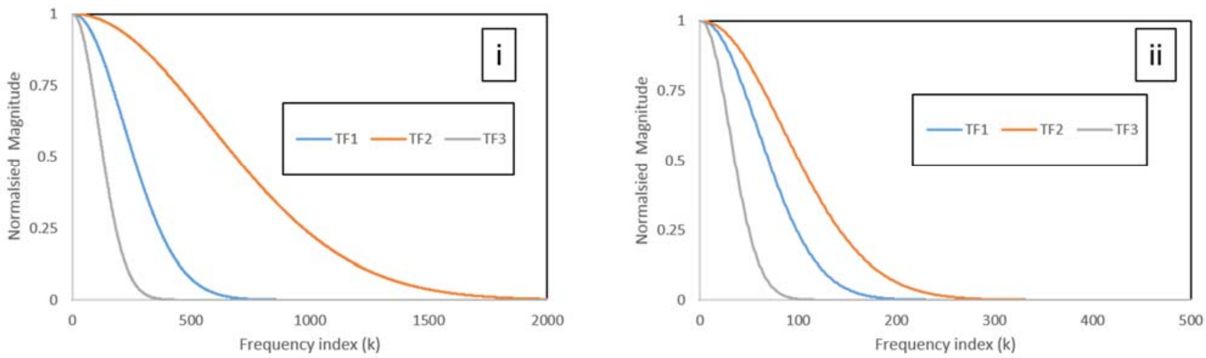

Figure 7. Variation in $\gamma(f)$ with variation in parameters a, b for (**i**) f = N/2, (**ii**) f = N/16.

Table 3. Test case to determine most suited values for a, b.

SL No	a	b	Case
1	10	0.5	TF1
2	1	0.1	TF2
3	20	1	TF3

Figure 8 shows the variation in localization window width ($\gamma(f)$) for different values of a, b as per Table 3. The veracity of these frequency windows is presented for f = N/2 (Figure 7i) and f = N/16 (Figure 7ii). In both instances, the window for FT1 lies between the corresponding ones for FT2 and FT3. This choice of parameters a, b will now be tested to determine their respective effects on temporal and frequency resolution.

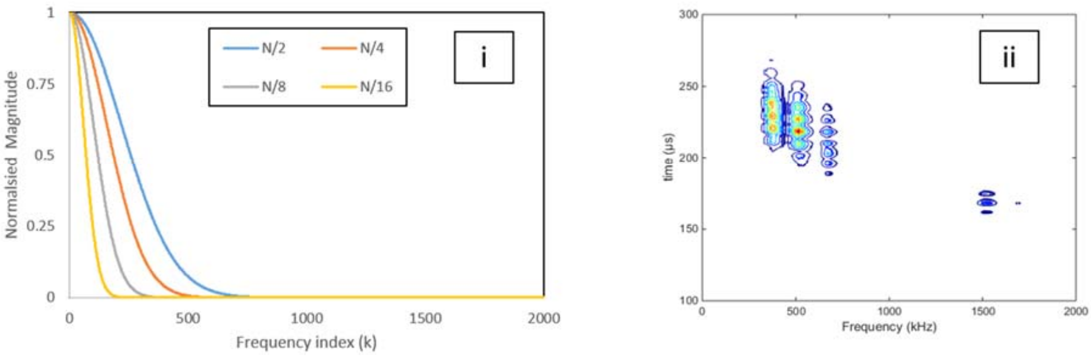

Figure 8. Effect of variation in localization window widths on time-frequency spectra for a = 10, b = 0.5 (**i**) Variation in $\gamma(f)$ and (**ii**) time-frequency spectra.

There is a clear separation in the arrival times of higher and lower frequency components (Figure 8). The higher frequencies travel faster and arrive at 165 µs. They are followed by the arrival of lower frequency components from 200 µs. Further, there is a subtle difference between the arrival times of the different components of the lower frequency components. Thus, a = 10 and b = 0.5 will be used as the parameters to scale the Gaussian window for the analysis of corrosion data in this work.

Clear improvement in the localization of time-frequency spectra can be observed in Figure 8ii. Features extracted through this improved paradigm of time-frequency analysis will be monitored as indicators for corrosion.

3.3. Guided Wave Modes

Time-frequency analysis indicates two prominent regions of spectral presence as shown in Figure 8ii. To develop a theoretical understanding of the guided wave modes, the system is modeled in Disperse software [58] as a cylindrical waveguide (steel bar) embedded in concrete. In the present model, the steel bar is 24 mm in diameter. It is surrounded by concrete of infinite length in the radial direction. The material properties of the steel and concrete used in the present study are presented in Table 4.

Table 4. Material properties of steel and concrete used to evaluate dispersion relations.

Properties	Steel	Concrete
Modulus, E (GPa)	210	29.6
Density (ρ) (kg/m^3)	7932	2200
Longitudinal attenuation (np/wl)	0.003	0.2
Shear attenuation (np/wl)	0.008	0.5
Poisson's ratio	0.286	0.27

It is imperative to select a suitable excitation frequency based on the modal propagation characteristics. Group velocity (Figure 9) and attenuation dispersion (Figure 10) curves will be paramount in the selection of excitation modes in the system. The guided wave modes with the lowest attenuation would propagate to the furthest distance, and the mode with maximum group velocity would arrive first. Judicious selection of the excitation frequency can limit the effects of dispersion and complications due to the interference of surrounding modes [59].

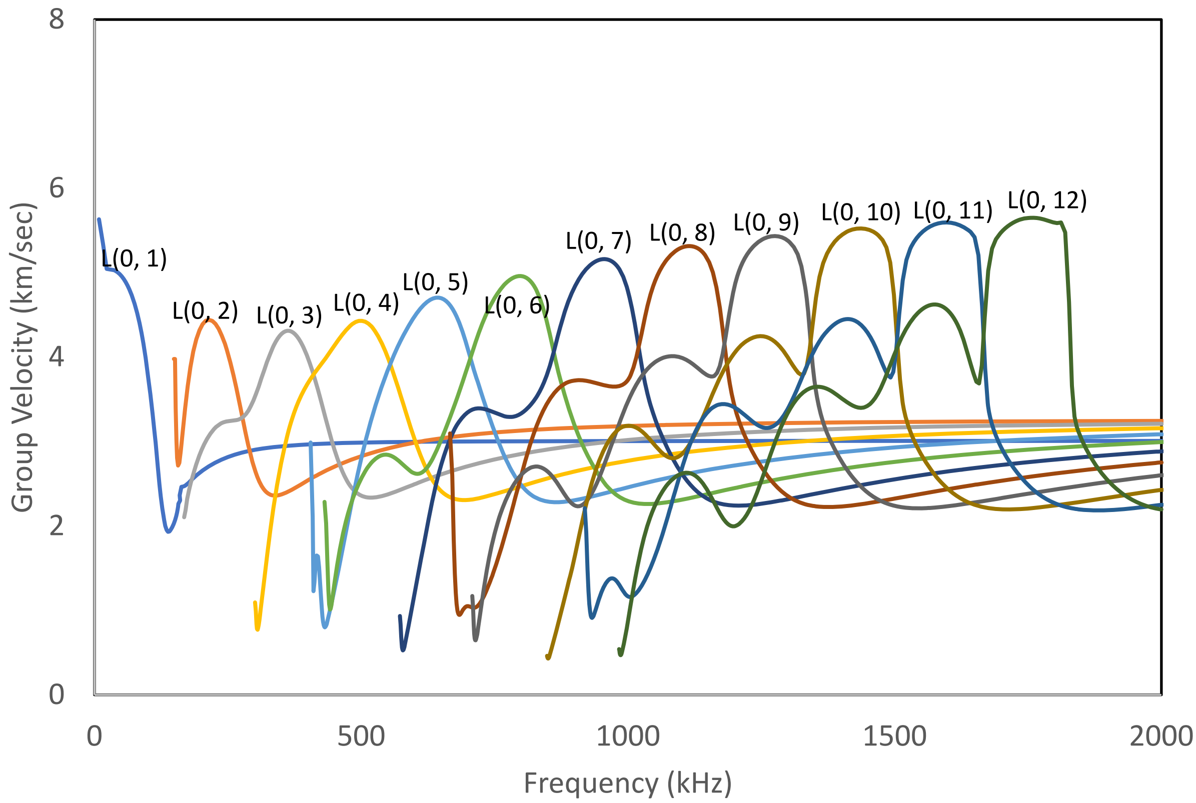

Figure 9. Group velocities of different longitudinal modes for a 24 mm steel bar in embodied concrete.

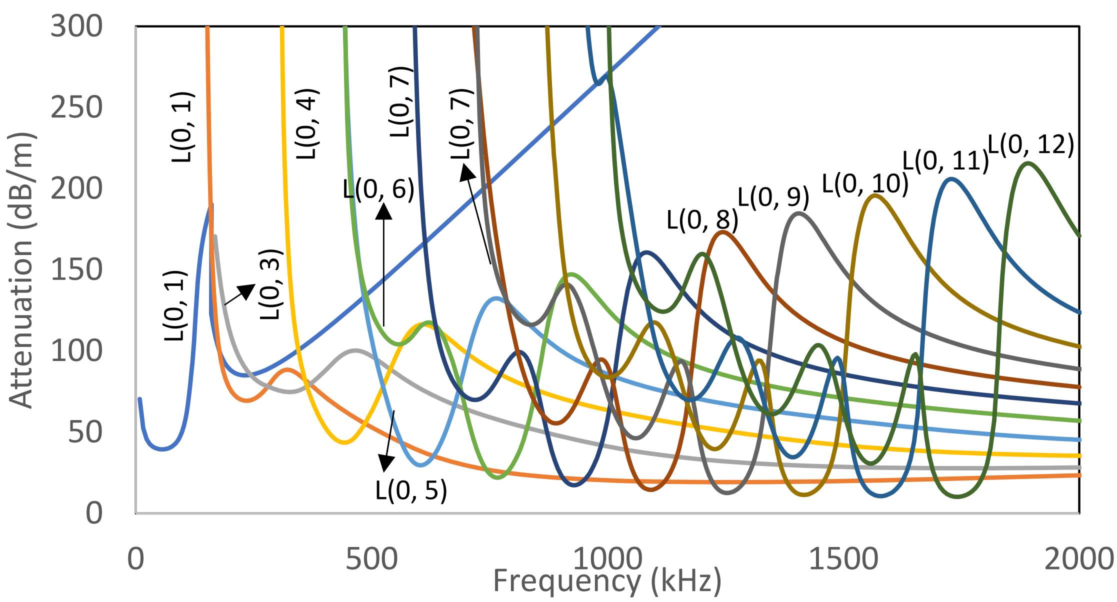

Figure 10. Attenuation dispersion curves of different longitudinal modes for a 24 mm steel bar in embodied concrete.

In the present case, a square pulse excitation of central frequency around 500 kHz was used. As a square pulse was used to excite the system, higher frequency components corresponding to the third harmonic of excitation were also induced in the system. Thus, longitudinal modes around 500 kHz and 1500 kHz were discerned. These two groups of frequencies will be analyzed herein.

To understand the effect of corrosion on the acquired signals, the group velocity dispersion curves are overlaid with the time-frequency spectra of the signal (Figure 8ii). Figure 11 reveals the guided wave modes being generated in the system. Clearly, two distinct groups of frequencies are observed. The higher frequencies corresponding predominantly to L(0, 10) and L(0, 11) modes and lower frequencies corresponding to L(0, 3), L(0, 4) and L(0, 5) are visible. A clear distinction between the higher and lower frequency guided wave modes is observed on account of the difference in their group velocities. The higher frequency modes traveling with a group velocity of 5400 m/s are distinct from the lower frequency modes that travel at 4500 m/s. Variations in the frequency modes and their corresponding velocities with induced corrosion warrant further exploration.

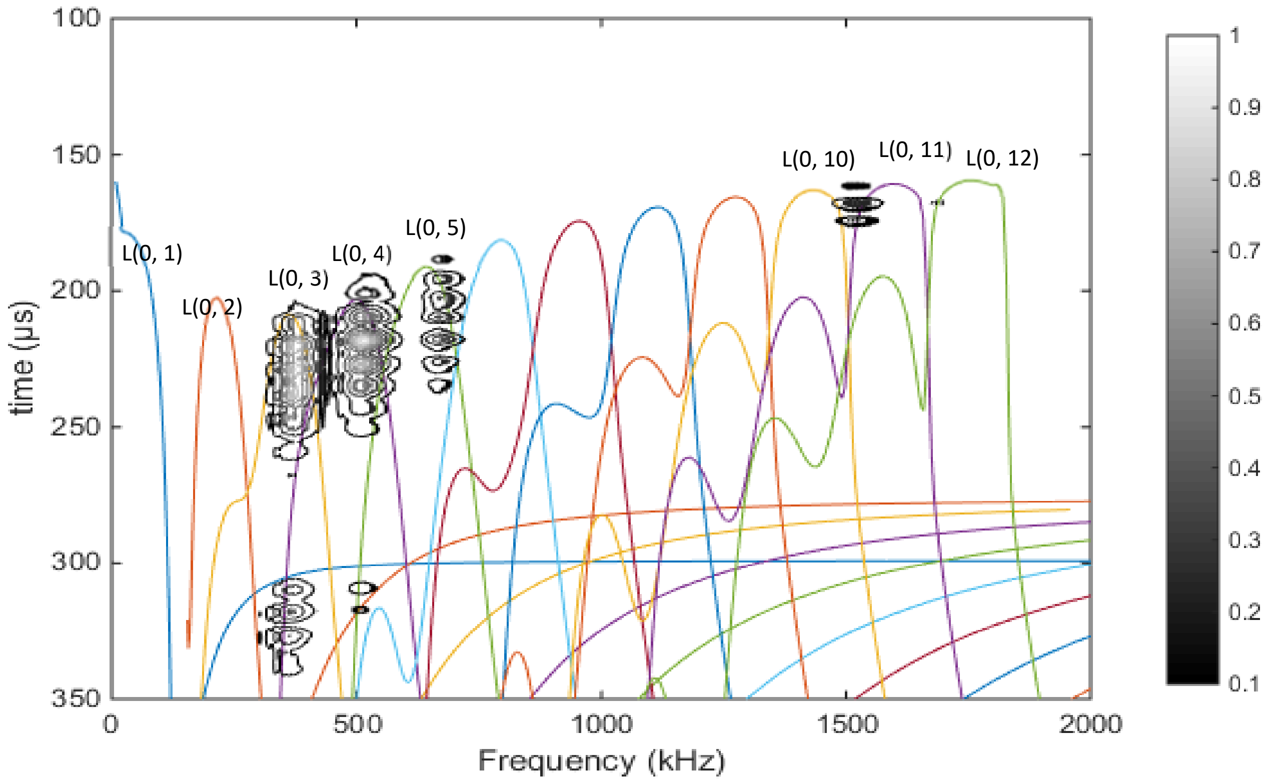

Figure 11. Spectral distribution over various guided wave modes in pristine condition for specimen S_{corr1}.

3.4. Variation of Guided-Wave Signal with Corrosion

Figure 12 presents the frequency spectra as the corrosion progresses. Between day 0 and day 5, the spectral iso-lines have become denser. This indicates an increase in the overall signal amplitude. Moreover, the component of the higher frequency modes has increased over the lower frequency modes. As a result, traces of L(0, 12) mode were observed alongside L(0, 10) and L(0, 11) modes. As the corrosion product is deposited at the steel–concrete interface, a soft layer of corrosion products separates the steel bar from the concrete [9]. This layer reduces the leakage of wave energy into the surrounding concrete [17]. After this time, a small brown patch of corrosion products on the concrete surface was observed, although no crack on the surface of the concrete was observed. From this point onwards, the signal amplitudes dropped steadily. The reduction in signal amplitude signifies the development of surface irregularities on the bar that scatters the waves.

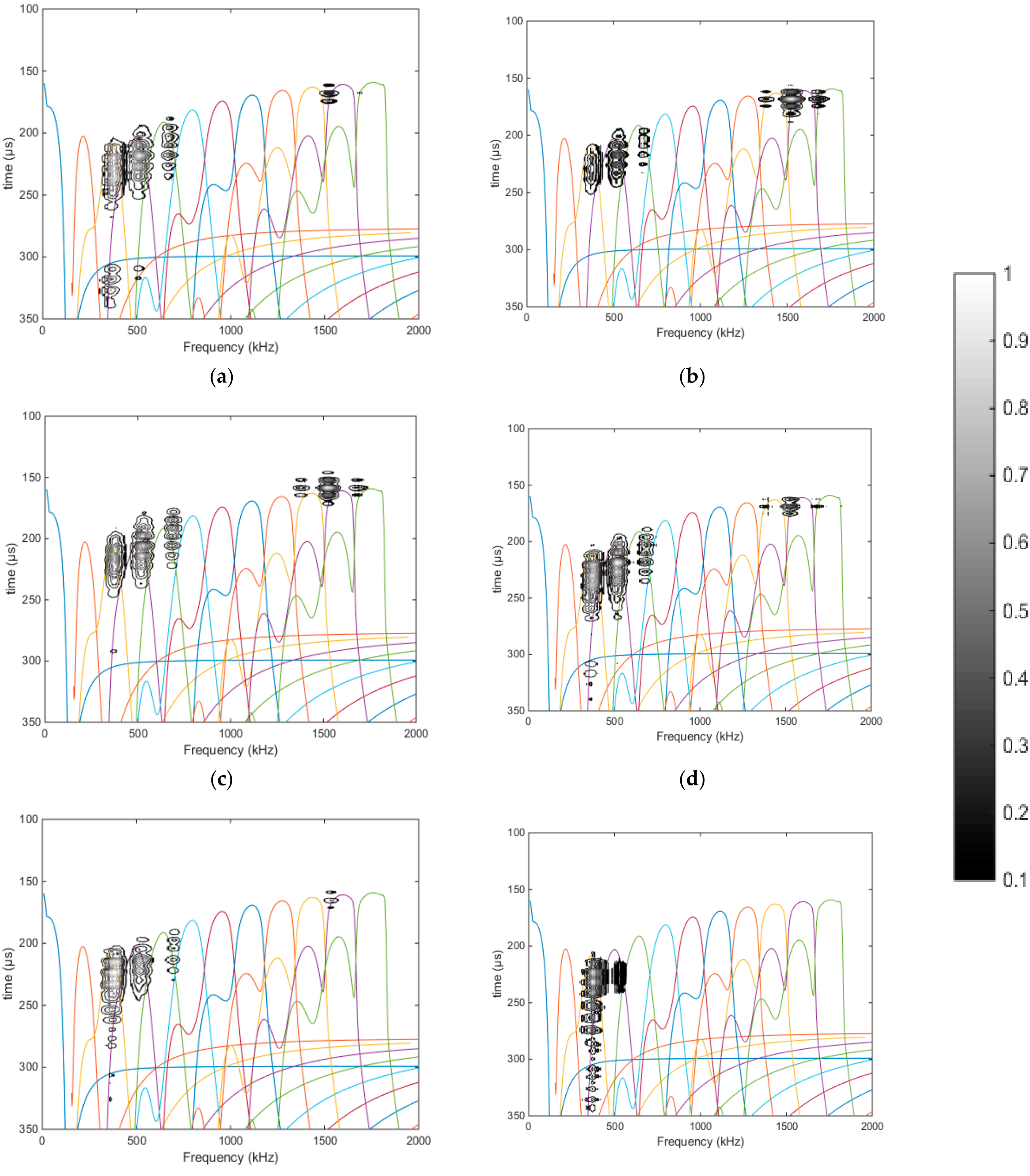

Figure 12. Variation in guided wave spectral content with progress in corrosion: (**a**) day 0, (**b**) day 5, (**c**) day 10, (**d**) day 18, (**e**) day 30, and (**f**) day 43.

Between day 5 and day 10 (Figure 12c), the signal amplitudes had dropped considerably. The loss was relatively higher in the lower frequency modes. On day 18 (Figure 12d), a considerable loss in the higher frequency modes was observed. From this stage onwards, both the higher frequency and lower modes attenuated steadily.

Subsequently, a thin crack on the surface of the concrete was visible. The corrosion product developed on the steel bar exerts a bursting pressure on the surrounding concrete. This resulted in the nucleation of longitudinal cracks along the length of the specimen. These cracks coalesced to form a longitudinal crack along with the rebar. On day 22, the longitudinal crack extended throughout the length of the specimen with a significant increase in oozing out of corrosion products. Subsequently, the higher frequency modes started to disappear. By day 30 (Figure 12e), they were insignificant. Past this point, only the lower frequency modes were discernible, and they too attenuated steadily. As higher frequency modes have smaller wavelengths, they are affected by small surface irregularities in the bar caused by corrosion. Among the lower frequency modes, L(0, 5) was the first to be affected. In this group, L(0, 5) has the highest frequency and hence the smallest wavelength. Thus, it is affected first when the surface irregularities reach the level of the wavelength of L(0, 5). Modes L(0, 3) and L(0, 4) were discernible until day 43. Differential attenuation of guided wave modes, especially between day 5 and day 18, requires further exploration. This warrants further investigation through an understanding of energy distribution for individual modes.

To understand the differential attenuation of higher and lower frequency modes to the condition of the waveguides, the energy distribution of these modes will be analyzed. As leakage of energy is significant in a layered system, it is important to distinguish the modes based on their energy distribution towards their center and at the surface. The energy distribution for the lower frequency modes (Figure 13a) at the concrete–steel interface is significantly greater than the higher frequency modes. The higher distribution of energy components towards the surface of the waveguide makes the lower frequency modes suited for the monitoring interface. The higher frequency modes (Figure 13b) have a considerable component of their modal energy concentrated around the core of the bar. A lower energy distribution at the surface of the waveguide makes them relatively less sensitive to variation in surface conditions up to ~2 mm from the interface. In this region, their attenuation is relatively unaffected due to local changes in the waveguide. Past this point, the modal energy significantly attenuates due to the local changes of the waveguide. As a result, the higher frequency components were significantly reduced only after day 18 of corrosion. On day 30, the higher frequency modes had attenuated significantly with the development of corrosion pits. The lower frequency modes had also started to attenuate past this point and this trend continued until the end of corrosion. The variation in guided wave signals will now be correlated with the acoustic signals to understand the progress of corrosion.

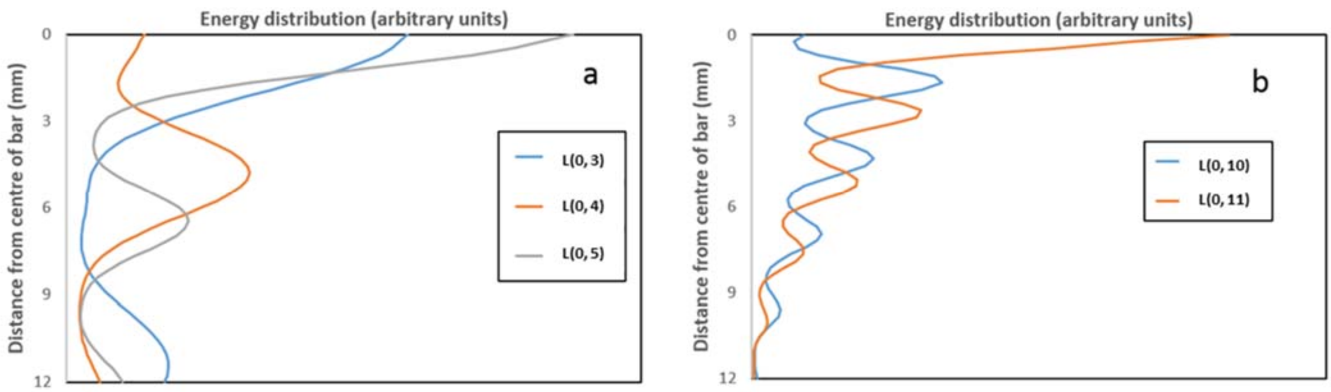

Figure 13. Total Energy density in guided wave modes (**a**) lower frequency modes (**b**) higher frequency modes.

3.5. Acoustic Emission Monitoring

The acoustic activity corresponding to different stages of corrosion will be studied through parameters such as energy, signal strength, and acoustic hits. They will be compared to the guided wave signals to determine the state of corrosion in the specimens. Acoustic sensors were attached to specimen S_{corr2}. Variations in cumulative energy and cumulative signal strength will be used as the acoustic parameters to understand the spread of corrosion. The cumulative signal strength (Figure 14a) indicates the variation in acoustic energy released during corrosion. The cumulative energy plot indicates the strength of the detected signal (Figure 14b). Acoustic hit data will supplement the other acoustic parameters to obtain a comprehensive understanding of the initiation and spread of corrosion. Key regions of inflection in the plot, also known as 'knee' regions, correspond to changes in energy and signal strength. They will be the key indicators for variations like corrosion.

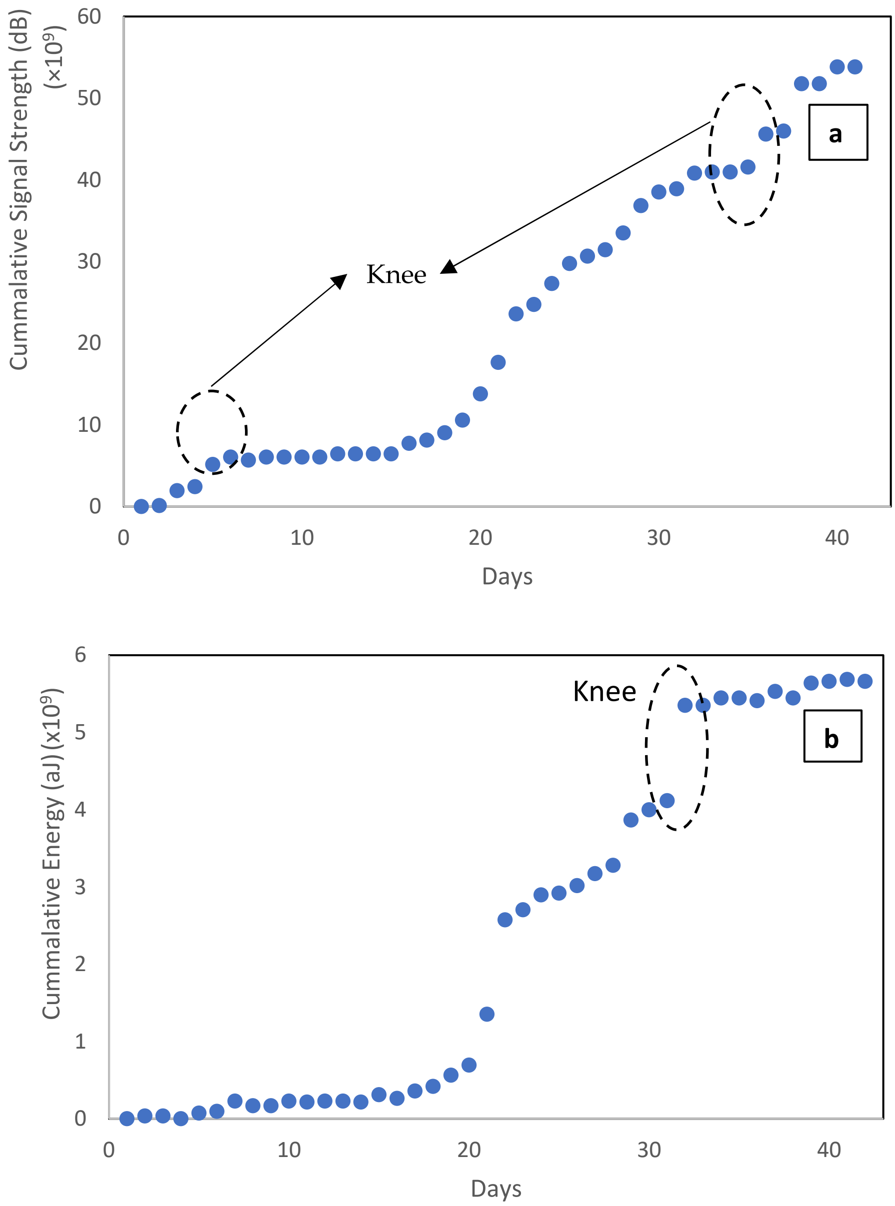

Figure 14. Variation in acoustic emissions was observed through (**a**) Cumulative Signal Strength and (**b**) Cumulative Energy during corrosion.

The thin adherent oxide layer around the rebar breaks as the rebar starts to corrode. With damage to this adherent oxide layer, corrosion product starts to develop between the rebar and concrete. As this corrosion product builds up, the cumulative signal strength and cumulative energy increase. On day 6, there was an increase in the slope of signal strength (Figure 14a). This change was greater in the case of cumulative acoustic signal strength compared to acoustic energy (Figure 14b). This can be attributed to the evolution of lower energy wave pulses of short duration originating from the corrosion product freely filling up the concrete–rebar interface.

As the corrosion product fills up the concrete–rebar interface, it exerts a bursting pressure on the surrounding concrete. Thus, at this stage, micro-cracking in the concrete around the rebar was predominant [45]. This increased signal strength and energy between day 6 and day 16. Pitting on the surface of the rebar commenced as the concrete surrounding the rebar cracked, thus leading to an increased ingress of chloride ions. Thus, after day 16, the slope of cumulative energy and signal strength increased at a greater rate until day 34. Here, the micro-cracks transitioned to macro-cracks. As a result of this transition, a longitudinal crack along with the specimen which had coalesced from these micro-cracks was observed on day 22. Past day 34, the specimen had already developed cracks due to the bursting pressure of the corroding rebar onto its surrounding concrete. As a result, the cumulative signal strength and energy increased marginally. This trend continued until the end of the experiments. Thus, transitions in the cumulative plot signify different stages of corrosion. To confirm and establish these regions, AE hits both from individual channels and a combination of all channels will now be studied.

Acoustic hits represent the detection of a signal on an acoustic sensor during the experiment. Following a consistent increase in acoustic hits, the first knee region was observed on day 6 when the corrosion product started to fill up the rebar–concrete interface. AE hits increased from this point onwards until day 34. The increment in slope increased significantly on day 16, thus representing the transition of cracks in the specimen from micro to macro. Past day 34, the increase in AE hits was marginal. Overall, this was consistent with the trend observed in Figure 15. Thus, the development of knee regions in acoustic activity corresponding to an increase in cracking as observed in the present study is consistent with that of past studies [45,60,61]. The variation in AE hits will now be further analyzed vis-à-vis guided wave signals and destructive tests to understand the state of condition in the specimen.

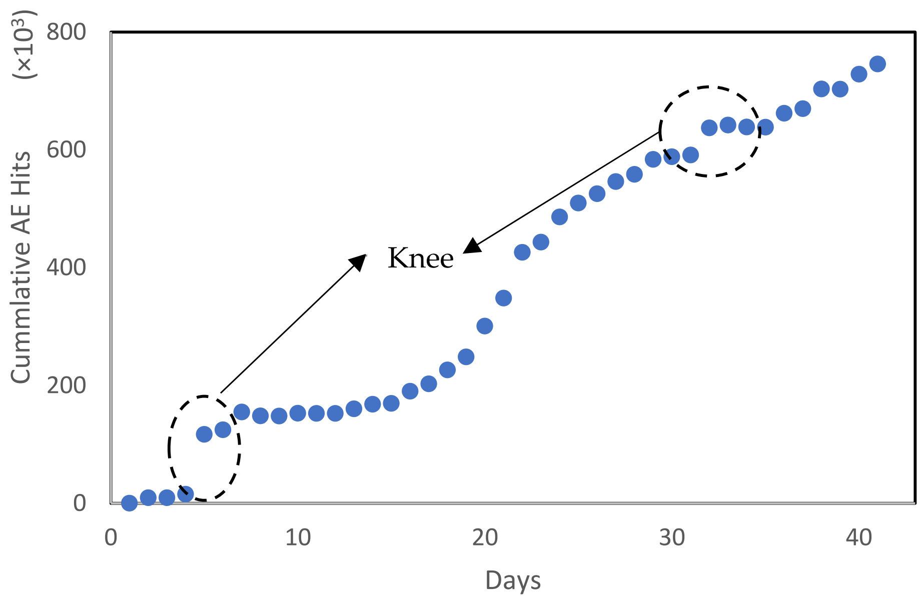

Figure 15. Variation in cumulative acoustic emissions hits during corrosion.

3.6. Destructive Tests

Destructive tests were performed to determine the variation in mechanical properties in the specimen due to corrosion. To conduct destructive tests, the steel bar was extracted from the concrete. It was thoroughly cleaned with a wire gauge. The mass loss to corrosion was determined by weighing the specimen. Profound pits on the corroded bar were observed on account of the material loss (Figure 16a,b). A total of 4.08% and 4.21% mass was lost due to corrosion in the case of S_{corr1} and S_{corr2}, respectively.

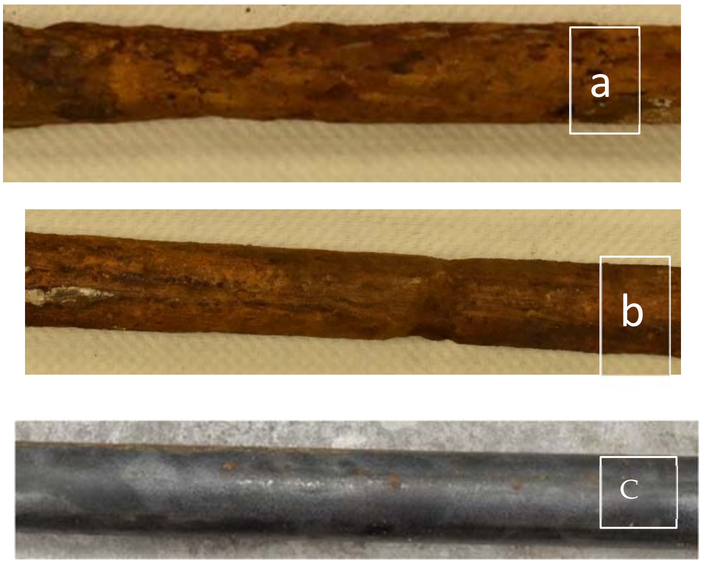

Figure 16. Comparison of specimen (**a**) S_{corr1} Corroded bar (**b**) S_{corr2} Corroded bar (**c**) pristine bar.

The extracted steel bar was subjected to a tensile test. These results were compared to the tensile test of a pristine specimen (Figure 17). A comparison of a pristine bar (Day 0) and the bar extracted after being subjected to 43 days of corrosion (Day 43) are presented. A reduction of 17.8% in yield strength and 35.28% in the ultimate strength due to corrosion was observed. The failure strain was reduced by 75.11%. A reduction of 15.26% in yield strength and 21.48% in the ultimate strength due to corrosion was observed for S_{corr2}. The failure strain was reduced by 72.28%.

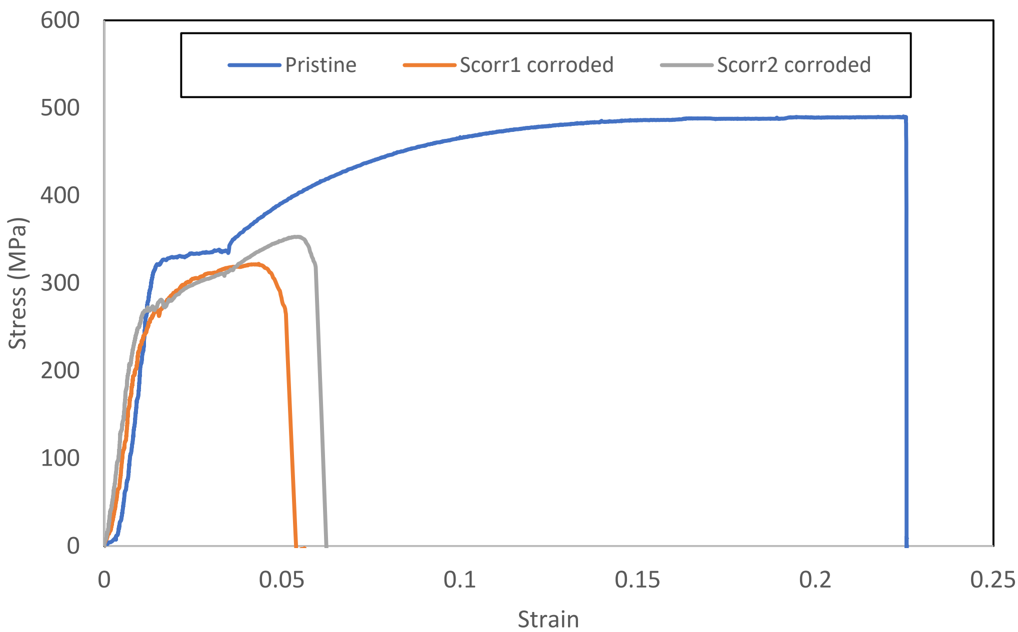

Figure 17. Stress–strain behavior of the steel bars in pristine condition and those extracted from specimens S_{corr1} and S_{corr2} after corrosion.

This indicates a severe loss in the ductility of the specimen due to corrosion, especially past the elastic region of the specimen. Reduction in cross-section locally due to corrosion can be attributed to the significant change in ductility due to corrosion. Thus, ductility and residual strength are reduced significantly to the progress of corrosion. A significant loss in ductility and residual strength was also observed in other corrosion studies [18,54].

4. Corrosion Classification

To quantify the effects of corrosion, time-frequency signal spectra obtained through Equation (12) were demarked into zones for lower and higher frequency components. Signal spectra in Zone A correspond to lower frequency modes and Zone B corresponds to higher frequency modes (Figure 18). The higher frequency components constitute primarily L(0, 10) and L(0, 11) modes under Zone B. The lower frequency components are comprised of L(0, 3), L(0, 4), and L(0, 5) modes under Zone A. The variation in spectral content in these regions is associated with ingress and the spread of corrosion. The spectral contribution in these zones will now be calculated by a spectral contribution parameter (χ_d) as per Equation (15).

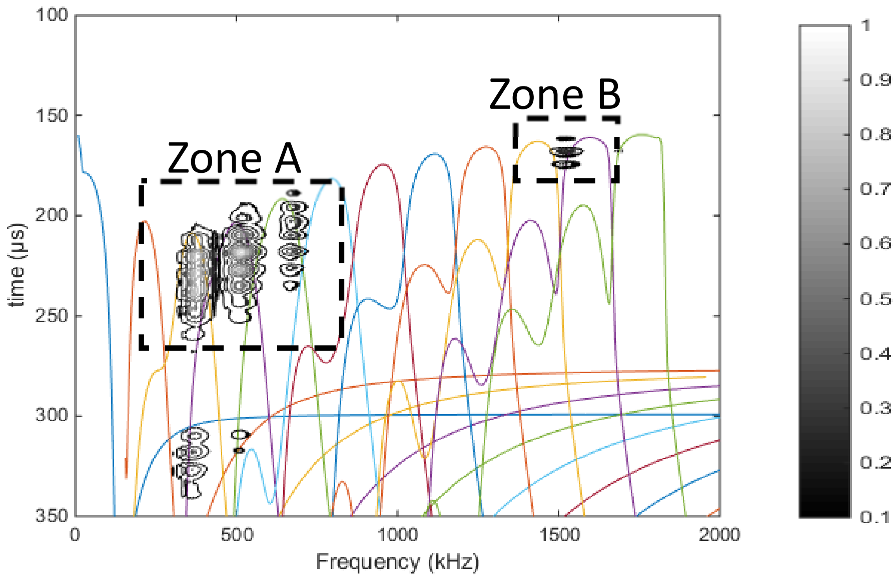

Figure 18. The spectral region corresponding to (**A**) lower and (**B**) higher frequency modes.

The trend for the spectral parameters for lower and higher frequencies will be reported as χ_{d_L} and χ_{d_H}, respectively. This parameter will be used to understand the spread of corrosion (Equation (13)).

$$\chi_d = \sum_{ii=t_l}^{t_h} \sum_{jj=f_l}^{f_h} S_{ca}(ii, jj) \tag{13}$$

Here, t_l, t_h represents the coordinates corresponding to lower and upper temporal limits of each Zone in S_{ca}. f_l, f_h represents the coordinates corresponding to the lower and upper-frequency limits in each Zone of S_{ca}. Coordinates to demarcate Zones A and B, selected as per their spectral presence, are presented in Table 5. These limits were selected based on the pixel intensities on the time-frequency plot.

Table 5. Parameters to calculate χ_d in Zone A and B.

Zone	t_l (μs)	t_h (μs)	f_l (kHz)	f_h (kHz)
Zone A	160	180	220	770
Zone B	190	280	1220	1650

The parameter χ_d is calculated distinctly for the spectral components of higher and lower frequencies. The spectral parameter for lower and higher frequencies are established as χ_{d_L} and χ_{d_H}, respectively. A relative spectral parameter (Equation (14)) will now be used to understand the variation in spectral trend and quantify attenuation in respective guided wave modes.

$$\chi_{RS} = \frac{\chi_{d\_H}}{\chi_{d\_L}} \tag{14}$$

To have a holistic basis for the variation in this trend, the parameter (χ_{RS}) is normalized to the maximum value among all stages of corrosion (χ_{RS_max}). Thus, χ_{RS_norm} is plotted as an index for the progress of corrosion (Equation (15)).

$$\chi_{RS\_norm} = \frac{\chi_{RS}}{\chi_{RS\_max}} \quad (15)$$

Figure 19 represents the variation of spectral content due to the progress of corrosion. An increase in χ_{RS_norm} marks the initiation of corrosion. This unanimous increase persisted until day 5 of corrosion. This indicates the build-up of corrosion products between rebar and concrete. With progress in corrosion, the layer of corrosion product breaks down. As a result, corrosion pits form on the rebar. This causes a slight decrease in χ_{RS_norm} past day 5. The falling trend is gradual past this point until day 10. As the modal energy concentration at the steel–concrete interface is relatively low, the effect of corrosion pits on the higher frequency modes is minimal (Figure 12).

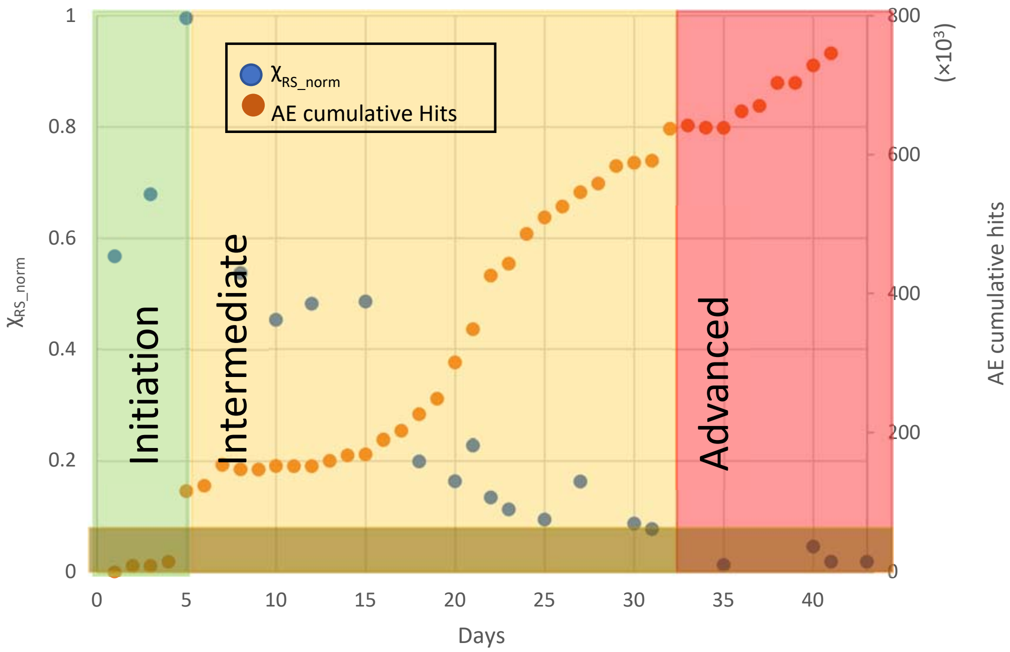

Figure 19. Relative variation in higher to lower frequency modes with progress in corrosion, indicating various stages of corrosion.

As the extent of corrosion pits increases to a few millimeters in depth, the higher frequency modes start to attenuate. This effect is profound with a sharp dip in χ_{RS_norm} past day 15. This marks an intermediate stage of corrosion. Significant attenuation beyond this point in the higher frequency modes has resulted in a sharp decrease in χ_{RS_norm}. The corrosion pits formed on the bar surface due to chloride ingress is a key factor in the observed signal attenuation. With a persistent falling trend, the magnitude of χ_{RS_norm} was reduced to an insignificant level from day 25. The heavy pitting of the bar was a key attribute of this stage of corrosion. The sensitivity of higher frequency guided wave modal components to the formation of a soft layer and the formation of surface pits were established. Thus, pitting due to corrosion has affected the ultrasonic signal characteristics as observed in previous studies [17,18]. This change depends upon the exciting guided-wave modes [62,63].

5. Conclusions

This paper explores the application of wave technologies and advanced signal processing for the nuanced monitoring of corrosion. Two concrete specimens (S_{corr1} and S_{corr2}) were subjected to accelerated corrosion. A nuanced time-frequency analysis was used to identify and associate guided wave modes with nucleation and spread of corrosion. A square pulse centered around 500 kHz excitation frequency was used to monitor specimen S_{corr1}. A series of lower frequency modes (centered on the excitation frequency) and higher frequency modes (thrice the excitation frequency) were generated. From the dispersion curves, the lower frequency modes corresponding to 305, 465, and 580 kHz were identified as L(0, 3), L(0, 4), and L(0, 5), respectively. The higher frequency modes at 1420 and 1560 kHz were identified as L(0, 10) and L(0, 11), respectively. A relative spectral parameter (χ_{RS_norm}) was established to determine the variation in the guided wave ultrasonics signal with progress in corrosion. Specimen S_{corr2} was monitored by acoustic emission through parameters such as hits, cumulative signal strength, and cumulative energy to supplement the guided wave data. Subsequently, the corroded steel bars were extracted from embedded concrete and their mechanical properties compared to that of a pristine steel bar.

Some key conclusions from the present research are the following:

- An initial increase in χ_{RS_norm} until day 6 signifies the improvement in signal strength past the onset of corrosion. This can be attributed to the formation of soft corrosion products around the rebar. In this duration, the cumulative AE parametric such as hits, signal strength, and energy were relatively low until this point. This represents the initiation of corrosion.
- After an initial increase in χ_{RS_norm}, its magnitude decreased past day 5. This decreasing trend continued until day 15. A steady rise in acoustic parameters in this duration indicates the nucleation of micro-cracks in the concrete surrounding the steel bar. χ_{RS_norm} decreased at a steeper gradient until day 34, which indicates the coalescence of micro-cracks to macro-cracks. At this stage, the acoustic parameters increase, indicating the evolution of macro-cracks. Thus, the intermediate stage of corrosion represents the transition of corrosion induction cracking in the concrete from micro-cracks to macro-cracks.
- Beyond day 34, as a consequence of profound pitting on the rebar and cracking in the concrete, the magnitude of χ_{RS_norm} was reduced to an insignificant value. During the same period, the increase in acoustic parameters was marginal. This trend continued until the conclusion of the experiment.
- A reduction in strength and ductility due to corrosion in the specimen was observed. The yield and ultimate strength of the specimen were reduced by 17.8% and 35.28%, respectively, and 15.26% and 21.48%, respectively, for S_{corr1} and S_{corr2} compared to the pristine specimen. Failure strain was reduced by 75.11% and 72.28%, respectively, for S_{corr1} and S_{corr2} due to corrosion.

The present experimental program demonstrates the efficacy of an advanced signal processing-based guided-wave ultrasonic system for monitoring different stages of corrosion. Acoustic emission parameters have supplemented the guided wave ultrasonic spectra towards identifying different stages of corrosion. Further experiments are on the way to establishing the veracity of the proposed method for variation in input waveform for the system.

Author Contributions: Conceptualization, S.M. and A.M.; methodology, S.M. and A.M.; software, S.M. and N.V.G.; validation, S.M. and L.K.A.; formal analysis, S.M. and L.K.A.; investigation, S.M., L.K.A. and A.M.; resources, S.M., L.K.A. and A.M.; data curation, S.M. and L.K.A.; writing—S.M.; writing—review and editing, A.M., N.V.G. and B.U.; visualization, S.M. and N.V.G.; supervision, A.M. and B.U.; project administration, S.M. and A.M.; funding acquisition, A.M. All authors have read and agreed to the published version of the manuscript.

Funding: This research received no external funding.

Institutional Review Board Statement: Not applicable.

Informed Consent Statement: Not applicable.

Conflicts of Interest: The authors declare no conflict of interest.

References

1. Mistri, A.; Bhattacharyya, S.K.; Dhami, N.; Mukherjee, A.; Barai, S.V. A Review on Different Treatment Methods for Enhancing the Properties of Recycled Aggregates for Sustainable Construction Materials. *Constr. Build. Mater.* **2020**, *233*, 117894. [CrossRef]
2. Australian Local Government Association. 2015 National State of the Assets Report. Available online: https://alga.com.au/national-state-of-the-assets-report-2015/ (accessed on 7 May 2022).
3. Wong, H.S.; Angst, U.M.; Geiker, M.R.; Isgor, O.B.; Elsener, B.; Michel, A.; Alonso, M.C.; Correia, M.J.; Pacheco, J.; Gulikers, J. Methods for Characterising the Steel–Concrete Interface to Enhance Understanding of Reinforcement Corrosion: A Critical Review by Rilem Tc 262-Sci. *Mater. Struct.* **2022**, *55*, 124. [CrossRef]
4. Ahmad, S. Reinforcement Corrosion in Concrete Structures, Its Monitoring and Service Life Prediction—-a Review. *Cem. Concr. Compos.* **2003**, *25*, 459–471. [CrossRef]
5. Liu, Y. Modeling the Time-to Corrosion Cracking of the Cover Concrete in Chloride Contaminated Reinforced Concrete Structures. Ph.D. Thesis, Virginia Tech, Blacksburg, VA, USA, October 1996.
6. Andrade, C.; Alonso, C.; Molina, F.J. Cover Cracking as a Function of Bar Corrosion: Part I-Experimental Test. *Mater. Struct.* **1993**, *26*, 453–464. [CrossRef]
7. Gadve, S.; Mukherjee, A.; Malhotra, S.N. Corrosion of Steel Reinforcements Embedded in Frp Wrapped Concrete. *Constr. Build. Mater.* **2009**, *23*, 153–161. [CrossRef]
8. Simon, P.D. Improved Current Distribution Due to a Unique Anode Mesh Placement in a Steel Reinforced Concrete Parking Garage Slab Cp System. In Proceedings of the CORROSION 2004, New Orleans, LA, USA, 28 March–2 April 2004.
9. Broomfield, J.P. *Corrosion of Steel in Concrete: Understanding, Investigation and Repair*; CRC Press: Oxon, UK, 2003.
10. Liang, M.-T.; Su, P.-J. Detection of the Corrosion Damage of Rebar in Concrete Using Impact-Echo Method. *Cem. Concr. Res.* **2001**, *31*, 1427–1436. [CrossRef]
11. Bagavathiappan, S.; Lahiri, B.B.; Saravanan, T.; Philip, J.; Jayakumar, T. Infrared Thermography for Condition Monitoring—A Review. *Infrared Phys. Technol.* **2013**, *60*, 35–55. [CrossRef]
12. Elsener, B.; Andrade, C.; Gulikers, J.; Polder, R.; Raupach, M. Hall-Cell Potential Measurements—Potential Mapping on Reinforced Concrete Structures. *Mater. Struct.* **2003**, *36*, 461–471. [CrossRef]
13. Song, H.-W.; Saraswathy, V. Corrosion Monitoring of Reinforced Concrete Structures-A. *Int. J. Electrochem. Sci.* **2007**, *2*, 1–28.
14. Achenbach, J. *Wave Propagation in Elastic Solids*; Elsevier: Amsterdam, The Netherlands, 2012; Volume 16.
15. Rose, J.L. *Ultrasonic Guided Waves in Solid Media*; Cambridge University Press: Cambridge, UK, 2014.
16. Graff, K.F. *Wave Motion in Elastic Solids*; Courier Corporation: North Chelmsford, MA, USA; Clarendon Press: Oxford, UK, 2012.
17. Sharma, S.; Mukherjee, A. Monitoring Corrosion in Oxide and Chloride Environments Using Ultrasonic Guided Waves. *J. Mater. Civ. Eng.* **2011**, *23*, 207–211. [CrossRef]
18. Sharma, S.; Mukherjee, A. Longitudinal Guided Waves for Monitoring Chloride Corrosion in Reinforcing Bars in Concrete. *Struct. Health Monit.* **2010**, *9*, 555–567. [CrossRef]
19. Liu, Y.; Ding, W.; Zhao, P.; Qin, L.; Shiotani, T. Research on in-Situ Corrosion Process Monitoring and Evaluation of Reinforced Concrete Via Ultrasonic Guided Waves. *Constr. Build. Mater.* **2022**, *321*, 126317. [CrossRef]
20. Mitra, M.; Gopalakrishnan, S. Guided Wave Based Structural Health Monitoring: A Review. *Smart Mater. Struct.* **2016**, *25*, 053001. [CrossRef]
21. Raghavan, A.; Cesnik, C.E.S. Finite-Dimensional Piezoelectric Transducer Modeling for Guided Wave Based Structural Health Monitoring. *Smart Mater. Struct.* **2005**, *14*, 1448. [CrossRef]
22. Sharma, S.; Mukherjee, A. Ultrasonic Guided Waves for Monitoring the Setting Process of Concretes with Varying Workabilities. *Constr. Build. Mater.* **2014**, *72*, 358–366. [CrossRef]
23. Na, W.B.; Kundu, T.; Ehsani, M.R. Ultrasonic Guided Waves for Steel Bar Concrete Interface Testing. *Ariel* **2002**, *129*, 31–248.
24. Sharma, A.; Sharma, S.; Sharma, S.; Mukherjee, A. Ultrasonic Guided Waves for Monitoring Corrosion of Frp Wrapped Concrete Structures. *Constr. Build. Mater.* **2015**, *96*, 690–702. [CrossRef]
25. Sharma, S.; Mukherjee, A. Monitoring Freshly Poured Concrete Using Ultrasonic Waves Guided through Reinforcing Bars. *Cem. Concr. Compos.* **2015**, *55*, 337–347. [CrossRef]
26. Wu, F.; Chan, H.-L.; Chang, F.-K. Ultrasonic Guided Wave Active Sensing for Monitoring of Split Failures in Reinforced Concrete. *Struct. Health Monit.* **2015**, *14*, 439–448. [CrossRef]
27. Ervin, B.L.; Kuchma, D.A.; Bernhard, J.T.; Reis, H. Monitoring Corrosion of Rebar Embedded in Mortar Using High-Frequency Guided Ultrasonic Waves. *J. Eng. Mech.* **2009**, *135*, 9–19. [CrossRef]
28. Ervin, B.L.; Reis, H. Longitudinal Guided Waves for Monitoring Corrosion in Reinforced Mortar. *Meas. Sci. Technol.* **2008**, *19*, 055702. [CrossRef]
29. Demma, A.; Cawley, P.; Lowe, M.; Roosenbrand, A.G.; Pavlakovic, B. The Reflection of Guided Waves from Notches in Pipes: A Guide for Interpreting Corrosion Measurements. *Ndt E Int.* **2004**, *37*, 167–180. [CrossRef]
30. Pavlakovic, B.N.; Lowe, M.J.S.; Cawley, P. High-Frequency Low-Loss Ultrasonic Modes in Imbedded Bars. *J. Appl. Mech.* **2001**, *68*, 67–75. [CrossRef]
31. Lowe, M.J.S.; Alleyne, D.N.; Cawley, P. Defect Detection in Pipes Using Guided Waves. *Ultrasonics* **1998**, *36*, 147–154. [CrossRef]

32. Sharma, S.; Mukherjee, A. Ultrasonic Guided Waves for Monitoring Corrosion in Submerged Plates. *Struct. Control. Health Monit.* **2015**, *22*, 19–35. [CrossRef]
33. Carbol, L.; Kusák, I.; Martinek, J.; Vojkůvková, P. Influence of Transducer Coupling in Ultrasonic Testing. Paper presented at the NDT in Progress 2015 VIIIth International Workshop. The e-Journal of Nondestructive Testing. Praha; Brno University of Technology, Brno, Czech Republic, 12–14 October 2015.
34. Cai, D.; Zou, C.; Sun, Z.; Zhou, Q.; Fu, Y.; Li, G. The Influence of Coupling Layer Thickness on Hollow Axles Ultrasonic Testing. In Proceedings of the 2015 International Conference on Control, Automation and Robotics, Singapore, 20–22 May 2015.
35. Gröchenig, K. *Foundations of Time-Frequency Analysis*; Springer Science & Business Media: New York, NY, USA, 2013.
36. Portnoff, M. Time-Frequency Representation of Digital Signals and Systems Based on Short-Time Fourier Analysis. *IEEE Trans. Acoust. Speech Signal Process.* **1980**, *28*, 55–69. [CrossRef]
37. Daubechies, I. The Wavelet Transform, Time-Frequency Localization and Signal Analysis. *IEEE Trans. Inf. Theory* **1990**, *36*, 961–1005. [CrossRef]
38. Prosser, W.H.; Seale, M.D.; Smith, B.T. Time-Frequency Analysis of the Dispersion of Lamb Modes. *J. Acoust. Soc. Am.* **1999**, *105*, 2669–2676. [CrossRef]
39. Abbate, A.; Koay, J.; Frankel, J.; Schroeder, S.C.; Das, P. Signal Detection and Noise Suppression Using a Wavelet Transform Signal Processor: Application to Ultrasonic Flaw Detection. *IEEE Trans. Ultrason. Ferroelectr. Freq. Control* **1997**, *44*, 14–26. [CrossRef]
40. Shelke, A.; Kundu, T.; Amjad, U.; Hahn, K.; Grill, W. Mode-Selective Excitation and Detection of Ultrasonic Guided Waves for Delamination Detection in Laminated Aluminum Plates. *IEEE Trans. Ultrason. Ferroelectr. Freq. Control* **2011**, *58*, 567–577. [CrossRef]
41. Burrows, S.E.; Dixon, S. Defect Detection Using a Scanning Laser Source. In *AIP Conference Proceedings 2011*; American Institute of Physics: New York, NY, USA, 2011.
42. Mostavi, A.; Kamali, N.; Tehrani, N.; Chi, S.-W.; Ozevin, D.; Ernesto, J.I. Wavelet Based Harmonics Decomposition of Ultrasonic Signal in Assessment of Plastic Strain in Aluminum. *Measurement* **2017**, *106*, 66–78. [CrossRef]
43. Majhi, S.; Mukherjee, A.; George, N.V.; Uy, B. Corrosion Detection in Steel Bar: A Time-Frequency Approach. *Ndt E Int.* **2019**, *107*, 102150. [CrossRef]
44. Majhi, S.; Mukherjee, A.; George, N.V.; Karaganov, V.; Uy, B. Corrosion monitoring in steel bars using laser ultrasonic guided waves and advanced signal processing. *Mech. Syst. Signal Process.* **2021**, *149*, 107176. [CrossRef]
45. Sharma, A.; Sharma, S.; Sharma, S.; Mukherjee, A. Investigation of Deterioration in Corroding Reinforced Concrete Beams Using Active and Passive Techniques. *Constr. Build. Mater.* **2018**, *161*, 555–569. [CrossRef]
46. Ohtsu, M. *Acoustic Emission and Related Non-Destructive Evaluation Techniques in the Fracture Mechanics of Concrete: Fundamentals and Applications*; Woodhead Publishing: Duxford, UK, 2015.
47. Shah, S.G.; Kishen, J.C. Use of acoustic emissions in flexural fatigue crack growth studies on concrete. *Eng. Fract. Mech.* **2012**, *87*, 36–47. [CrossRef]
48. Grosse, C.U.; Ohtsu, M. *Acoustic Emission Testing*; Springer Science & Business Media: Berlin/Heidelberg, Germany, 2008.
49. Di Benedetti, M.; Loreto, G.; Matta, F.; Nanni, A. Acoustic Emission Monitoring of Reinforced Concrete under Accelerated Corrosion. *J. Mater. Civ. Eng.* **2013**, *25*, 1022–1029. [CrossRef]
50. Di Benedetti, M.; Loreto, G.; Matta, F.; Nanni, A. Acoustic Emission Historic Index and Frequency Spectrum of Reinforced Concrete under Accelerated Corrosion. *J. Mater. Civ. Eng.* **2014**, *26*, 04014059. [CrossRef]
51. Zaki, A.; Chai, H.K.; Behnia, A.; Aggelis, D.G.; Tan, J.Y.; Ibrahim, Z. Monitoring Fracture of Steel Corroded Reinforced Concrete Members under Flexure by Acoustic Emission Technique. *Constr. Build. Mater.* **2017**, *136*, 609–618. [CrossRef]
52. Yuyama, S.; Nishida, T. Acoustic Emission Evaluation of Corrosion Damages in Buried Pipes of Refinery. *J. Acoust. Emisison* **2003**, *21*, 187–194.
53. Ohtsu, M.; Tomoda, Y. Phenomenological Model of Corrosion Process in Reinforced Concrete Identified by Acoustic Emission. *ACI Mater. J.* **2008**, *105*, 194–199.
54. Sharma, A.; Sharma, S.; Sharma, S.; Mukherjee, A. Monitoring Invisible Corrosion in Concrete Using a Combination of Wave Propagation Techniques. *Cem. Concr. Compos.* **2018**, *90*, 89–99. [CrossRef]
55. Uddin, A.K.M.F.; Numata, K.; Shimasaki, J.; Shigeishi, M.; Ohtsu, M. Mechanisms of Crack Propagation Due to Corrosion of Reinforcement in Concrete by Ae-Sigma and Bem. *Constr. Build. Mater.* **2004**, *18*, 181–188. [CrossRef]
56. Sahu, S.S.; Panda, G.; George, N.V. An Improved S-Transform for Time-Frequency Analysis. In Proceedings of the 2009 IEEE International Advance Computing Conference, (IACC) 2009, Patiala, India, 6–7 March 2009.
57. Agrawal, S.; George, N.V.; Prashant, A. Gpr Data Analysis of Weak Signals Using Modified S-Transform. *Geotech. Geol. Eng.* **2015**, *33*, 1167–1182. [CrossRef]
58. Pavlakovic, B.; Lowe, M.; Alleyne, D.; Cawley, P. Disperse: A General Purpose Program for Creating Dispersion Curves. In *Review of Progress in Quantitative Nondestructive Evaluation*; Plenum Press: New York, NY, USA, 1997; pp. 185–192.
59. Beard, M.D.; Lowe, M.J.S.; Cawley, P. Ultrasonic Guided Waves for Inspection of Grouted Tendons and Bolts. *J. Mater. Civ. Eng.* **2003**, *15*, 212–218. [CrossRef]
60. Zaki, A.; Chai, H.K.; Aggelis, D.G.; Alver, N. Non-Destructive Evaluation for Corrosion Monitoring in Concrete: A Review and Capability of Acoustic Emission Technique. *Sensors* **2015**, *15*, 19069–19101. [CrossRef]

61. Kawasaki, Y.; Wakuda, T.; Kobarai, T.; Ohtsu, M. Corrosion Mechanisms in Reinforced Concrete by Acoustic Emission. *Constr. Build. Mater.* **2013**, *48*, 1240–1247. [CrossRef]
62. Sriramadasu, R.C.; Banerjee, S.; Lu, Y. Sensitivity of Longitudinal Guided Wave Modes to Pitting Corrosion of Rebars Embedded in Reinforced Concrete. *Constr. Build. Mater.* **2020**, *239*, 117855. [CrossRef]
63. Rajeshwara, C.S.; Banerjee, S.; Lu, Y. Identification of Zero Effect State in Corroded Rcc Structures Using Guided Waves and Embedded Piezoelectric Wafer Transducers (Pwt). *Procedia Eng.* **2017**, *188*, 209–216. [CrossRef]